Available online at www.sciencedirect.com
ScienceDirect
Journal of Catalysis 248 (2007) 235–248
JOURNAL OF CATALYSIS
www.elsevier.com/locate/jcat

Propene epoxidation over Au/Ti-SBA-15 catalysts

Elena Sacaliuc [a], Andrew M. Beale [a], Bert M. Weckhuysen [a,*], T. Alexander Nijhuis [b,*]

[a] *Inorganic Chemistry and Catalysis Group, Department of Chemistry, Faculty of β Sciences, Utrecht University, Sorbonnelaan 16, 3584 CA Utrecht, The Netherlands*

[b] *Department of Chemical Reactor Engineering, Eindhoven University of Technology, Den Dolech 2 Helix, STW 1.26, P.O. Box 513, 5600 MB Eindhoven, The Netherlands*

Received 1 February 2007; revised 10 March 2007; accepted 13 March 2007

Available online 25 April 2007

Abstract

Highly dispersed gold nanoparticles were synthesized within the channels of a mesoporous Ti-SBA-15 support, followed by thorough catalyst characterization and testing in the selective epoxidation of propene to propene oxide. For this purpose, two series of Ti-SBA-15 materials differing in their Ti content were prepared by either grafting or direct synthesis. The resulting Au/Ti-SBA-15 catalyst materials were characterized by X-ray fluorescence (XRF), X-ray diffraction (XRD), transmission electron microscopy (TEM), nitrogen sorption, UV–visible diffuse reflectance spectroscopy (UV–vis DRS), and X-ray absorption spectroscopy (EXAFS and XANES) at both the Ti K and Au L_3 edges. The catalytic performance of the Au/Ti-SBA-15 materials was been evaluated in the direct epoxidation of propene using a mixture of H_2 and O_2. The reaction data indicate that Au/Ti-SBA-15 materials obtained by Ti grafting have greater catalytic activity than the samples in which Ti-SBA-15 was obtained by direct synthesis. These differences in catalytic behavior are attributed to differences in the amount and dispersion of Ti within the mesoporous silica support, as well as to differences in the Au nanoparticle size, and are discussed in relation to data obtained previously for Au/TiO_2 catalysts.

Keywords: Epoxidation; Propene oxide; Gold; Au/Ti-SBA-15; Metal–support interaction

1. Introduction

The development of an efficient catalyst for the production of propene oxide is an industrially important but challenging task [1]. Propene oxide is a very important intermediate for the synthesis of commercial products, including adhesives, paints, and cosmetics. The current methods used for propene oxide synthesis—the chlorhydrin and hydroperoxide processes—have important disadvantages. The chlorhydrin process involves the production of chlorinated side products and calcium chloride waste, whereas the hydroperoxide process produces a stoichiometric amount of co-product. Thus, a process in which a catalyst could directly epoxidize propene using only oxygen or air is highly desirable [1]. The traditional Ag-on-α-alumina catalysts, which are used on a large scale in industry for the epoxidation of ethene, have a low selectivity for the propene epoxidation, primarily because of the reactivity of the γ-hydrogen atoms. Haruta et al. discovered that a catalytic system consisting of highly dispersed gold on a titania support was capable to directly epoxidize propene with a mixture of hydrogen and oxygen under mild conditions [2]. Previously, this catalytic system was known mostly for its high activity in the CO oxidation at ambient temperatures [3].

The surprisingly high catalytic activity of gold, which was traditionally considered a chemically inert element, in the direct epoxidation of propene with hydrogen and oxygen attracted a considerable academic and industrial interest. This is clear from, for example, the great number of scientific publications on this topic [4]. Despite this attention, the mode of operation of these catalysts in epoxidation of propene is still unclear, and several reaction mechanisms have been proposed. In all cases, it was observed that both the presence of gold and titania is necessary to have reasonable propene epoxidation activity [5,6]. Although gold-on-titania (Au/TiO_2) catalysts are very selective in this reaction (>90%), these systems still need considerable improvements to be made attractive for application in a large-

* Corresponding authors. Faxes: +31 302511027, +31 402446653.
E-mail addresses: b.m.weckhuysen@chem.uu.nl (B.M. Weckhuysen), t.a.nijhuis@tue.nl (T.A. Nijhuis).

0021-9517/$ – see front matter
doi:10.1016/j.jcat.2007.03.014

scale industrial process. The low activity (1–2%) and related PO yield, hydrogen efficiency (30%), and catalyst stability are the main problems to be tackled [7,8]. To do so, several factors have been investigated. An active part of the catalyst was found to be the support oxide, and various Ti-based metal oxides with distinct crystalline structures and porosities have been used for supporting Au nanoparticles [8–19]. Production of propylene oxide was found to be influenced by the crystalline nature of the supports, the anatase form of titanium dioxide resulted in PO formation; in contrast, the rutile structure and amorphous TiO_2 caused complete oxidation to CO_2 [9]. Nonporous silica has been used to support Ti and Au; however, an ideal activity has not been achieved. A high temperature is required to create the tight bonding Ti–O–Si connection embedded in the silica matrix, which is necessary for PO selectivity besides supported Au nanoparticles [20].

Titanium silicalite-1 (TS-1) is an excellent propene epoxidation catalyst when hydrogen peroxide is used as an oxidant. When gold nanoparticles are supported on TS-1, the catalytic materials are active in direct propene epoxidation; however, at low temperature, these materials are less active than the related Au/TiO_2 catalysts. Assuming that the activity is comparable in the sites, a higher reaction temperature is needed to reach a conversion identical to that of the Au/TiO_2 catalyst. On the other hand, the main advantage of gold nanoparticles on a TS-1 support is their ability to resist deactivation and to achieve a higher selectivity at higher reaction temperature [21]. The difference in activity between TS-1- and TiO_2-based catalysts can be explained by the presence of isolated Ti sites, whereas the lower reactivity of Si–OH sites that neighbor the active site leads to improved catalyst durability. Ti has also been incorporated in catalyst materials with high surface areas, such as mesoporous MCM-41 and MCM-48 supports, using different preparation techniques, including hydrothermal synthesis and sol–gel procedures [8,13–16]; it was found that the increase in epoxide yield is dependent of the method and amount of Ti incorporated in the mesoporous silica.

Along with well-dispersed tetrahedral-coordinated Ti sites in a silica matrix, the size of the gold nanoparticles also is important for an active catalyst. Ion exchange [21], deposition–precipitation [20,22,23], and impregnation [24] are a few of the synthesis procedures that have been used to create well-dispersed Au nanoparticles on Ti-based support oxides. Interestingly, the most frequently used method to obtain suitable nanosized gold particles is the deposition–precipitation process.

Haruta et al. [25,26] have shown that the optimal gold nanoparticles size for propene epoxidation is 2–5 nm. Gold nanoparticles with a smaller dimension catalyze the hydrogenation of propene to propane, whereas those with larger dimensions increase the selectivity to combustion. Haruta el al. [27] claims that the requirements for the epoxidation for propene involves isolated Ti sites combined with Au nanoparticles with sizes between 2–4 nm, support oxides with mesopores higher then 5 nm for the effective dispersion of Au nanoparticles inside the pores, and good support hydrophobicity for better propylene oxide desorption. Considering the possible type of support oxides that could meet these requirements mesoporous modified Ti-SBA-15 is a suitable option. SBA-15 was first synthesized by Zhao et al. [28], using a triblock copolymer surfactant as a template. SBA-15 is a mesoporous silica with uniform hexagonal channels ranging from 50 to 300 Å and a surface area $>700\ m^2/g$. The main advantages of SBA-15 over MCM-41 materials are the higher hydrothermal stability, thicker walls, and larger pore size [28,29]. Ti-SBA-15 has been synthesized using different procedure [30–32] and used for selective oxidation of various organic compounds in liquid phase with hydrogen peroxide as oxidant.

To the best of our knowledge, no reports regarding the deposition of Au on Ti-SBA-15 have been published to date. Therefore, here we report on the synthesis of Au/Ti-SBA-15 materials using two different preparation routes for the SBA-15 support oxide; that is, Ti was incorporated in the SBA-15 structure by either direct hydrothermal synthesis or a grafting procedure. Later, Au was introduced to the Ti-SBA-15 material by the deposition–precipitation method. We investigate in detail the influence of preparation method on the final catalyst structure and its catalytic activity in the epoxidation of propene with a hydrogen and oxygen mixture.

2. Experimental

2.1. Catalyst preparation

Preparation of Ti-SBA-15 supports used the following chemicals: tetraethylorthosilicate (TEOS, Aldrich, 98%), triblock copolymer, poly(ethylene glycol)–poly(propylene glycol)–poly(ethylene glycol) (PPE–PPG–PPE) (Aldrich), isopropanol (Aldrich, >99.5%), titanium isopropoxide (Across, 98%), titanium(IV) oxyacetylacetonate monohydrate (Aldrich, p.a.), and hydrogen tetrachloroaurate(III) solution $HAuCl_4$ (17 wt% in dilute HCl, Aldrich). Ti was incorporated into the mesoporous SBA-15 material by two routes: direct synthesis and grafting. The catalyst supports prepared by hydrothermal Ti incorporation are designated TiH-*n*, whereas those prepared by Ti grafting are designated TiG-*n*, were *n* is the Si/Ti molar ratio. The preparation of mesoporous silica SBA-15 was carried out according to the method of Zhao et al. [28,29]. In the synthesis procedure, amphiphilic triblock copolymer, poly(ethylene glycol)–poly(propylene glycol)–poly(ethylene glycol), was first dissolved in aqueous acidic solution in deionized water and hydrochloric acid (Merck, 37%) under continuous stirring. The mixture was heated at 40 °C for 12 h before TEOS was slowly added under vigorous magnetic stirring. The gel, with a molar composition of 1.00 SiO_2/0.01 PEG–PPG–PEG/4.77 HCl/152.79 H_2O, was stirred for another 10 h and then transferred into a Teflon-lined steel autoclave and kept at 100 °C under static conditions for 24 h. The resulting solid was filtered, washed with deionized water, dried in open air, and calcined in static air at 550 °C for 6 h at a heating rate of 2 °C/min to decompose the triblock copolymer.

Titanium-grafted SBA-15 samples with different Si/Ti molar ratios (10, 20, 40, and 80) were prepared by dry impregnation using titanium isopropoxide as a titanium source [33]. Titanium was loaded into the SBA-15 support oxide under an N_2

atmosphere in a glovebox at room temperature. Then 2 g of SBA-15 was impregnated with a 6-mL solution of titanium isopropoxide in dry isopropanol. The solvent was removed from impregnated materials under flowing nitrogen at room temperature for 48 h. The Ti-SBA-15 samples were calcined at 400 °C for 4 h. In addition, a series of Ti-SBA-15 materials with varying Si/Ti molar ratios between 10 and 80 were synthesized hydrothermally [34]. TEOS and titanium(IV) oxyacetylacetonate monohydrate were been used as silicon and titanium sources, respectively. The triblock copolymer (PEG–PPG–PEG) was used as the structure-directing agent, whereas concentrated HCl was used to adjust the pH. The synthesis was carried out similarly as for pure SBA-15, but with the Ti source added after the introduction of TEOS. The titanium(IV) oxyacetylacetonate was predissolved in a solution of isopropanol. The resulting samples were washed with deionized water and dried overnight at 60 °C. Once dry, the resulted white powder was calcined at 550 °C for 6 h.

The 1% Au catalysts were prepared via a deposition–precipitation method [11] in which the gold precursor, $HAuCl_4$, was precipitated on the supports by increasing the pH to 9.5. A solution of chloroauric acid in water was slowly added to a stirred suspension of 2 g of Ti-SBA-15 support in water. The pH of the solution was kept at 9.3 with aqueous ammonia (Merck, 25%), and the solution was aged for 30 min at the room temperature. The catalyst was washed repeatedly with distilled water, dried in air overnight at 60 °C, and calcined at 400 °C for 4 h.

2.2. Catalyst characterization

The degree of crystallinity and morphology of the obtained Au/Ti-SBA-15 materials were characterized using transmission electron microscopy (TEM) and X-ray diffraction (XRD). The latter was performed using a Bruker-AXS D8 Advance powder X-ray diffractometer, equipped with automatic divergence slit, Våntec-1 detector, and cobalt $K\alpha_{1,2}$ ($\lambda = 1.79026$ Å) source. TEM images were obtained using an FEI Tecnai 20F transmission electron microscope operated at 200 keV, with a Schottky field emission gun and a twin objective lens. The magnification range was 25–700 k, the point-to-point resolution was 0.27 nm, and the lattice image resolution was 0.14 nm. The specific surface area and pore volume were determined by N_2 sorption measurements with a Micromeritics ASAP 2400 instrument. Surface areas were calculated using the BET model with micropores and macropores described by the Horvath–Kawazoe and BJH models, respectively. UV–vis DRS measurements were carried out at room temperature on a Varian Cary 500 instrument in the range of 200–2200 nm. This setup was equipped with a diffuse reflectance accessory set to collect diffuse reflected light only. The scan was made with an averaging time of 1 s, a data interval of 1 nm, and a scan rate of 60 nm/min. A baseline correction was performed using a white Halon standard. Ti K-edge and Au L_3-edge XAFS measurements were carried out on station BM26A at the ESRF (Grenoble, France) operating at 6 GeV with a typical current of 150–250 mA. The station was equipped with a Si(111) double-crystal monochromator, followed by two vertically focusing Pt- and Si-coated mirrors for harmonic rejection. X-ray absorption spectra were recorded using ion chambers for measuring incident and transmitted beam intensities and a nine-element monolithic germanium detector for fluorescence measurements. The maximum in the first derivative plot for the Ti (4966.4 eV) and Au (11918.7 eV) foil data was used to calibrate the monochromator position. In a typical experiment, about 100 mg of sample was pressed to form self-supporting wafers before being mounted in a specialized cell for recording XAFS data. The samples were then dehydrated at 300 °C. Measurements were performed at room temperature in normal step scanning mode; multiple scans were obtained to improve the signal-to-noise ratio. For the Ti K-edge measurements, a step size of 0.2 eV/point over an energy range of 4964–4990 eV was used to obtain detailed information on the pre-edge feature at ca. 4969.2 eV. This peak was then profiled using a Lorentzian function to extract information on its position and intensity, which was then used to obtain indirect information on the proportion of tetrahedral Ti^{4+} species in the samples. The XAFS data were processed using the suite of programs available at Daresbury Laboratory, namely EXCALIB (for converting the raw data to an energy vs absorption coefficient), EXBROOK (for normalization of XANES data at 20 eV above the absorption edge and background subtraction to extract EXAFS) and EXCURV98 (to perform a least squares fitting analysis of the data to extract more detailed local structural details) [35]. An amplitude reduction factor (S_0^2) value of 0.83, obtained from fitting the FCC-structured Au foil with a fixed coordination number(s) up to the fourth shell, also was used in the analysis. Multiple scattering contributions were considered when fitting the higher shells but were found to be significant only for simulating amplitude-related information when fitting the fourth shell and thus were ignored when obtaining coordination numbers for the second and third shells.

2.3. Catalyst testing

A flow reactor was used to determine the catalytic performance of the different catalysts prepared. Typically, the experiments were carried out with 0.4 g of catalyst material and a flow of 50 N mL/min. The gas mixture consisted of 10% oxygen, 10% hydrogen, and 10% propene in helium. Analysis of the gas leaving the reactor was carried out using an Interscience Compact gas chromatography system, equipped with a Molsieve 5A and a Porabond Q column, each with a thermal conductivity detector (TCD). Gas samples were analyzed every 3 min. The experiments were carried out in cycles of 5 h at reaction temperature with the reactant mixture, followed by a regeneration cycle. In regeneration, 10% oxygen in helium was used. The catalyst was heated to 300 °C and kept there for 1 h, after which it was cooled to the next reaction temperature in the cycle. The catalytic test was typically performed at 10–15 different temperatures (including duplicates) to determine the deactivation pattern for each catalyst. During the catalytic tests, UV–vis measurements were performed in situ at 250–1100 nm using an Avantes Avaspec-2048-4 spectrometer.

Table 1
Summary of the characterization results of the different SBA-15, Ti-SBA-15 and Au/Ti-SBA-15 samples prepared in the frame of this study (na = not applicable)

Sample	Si/Ti (initial gel)	Si/Ti (final product)	BET surface area (m^2/g)	Micropore volume (cm^3/g)	Pore volume BJH (cm^3/g)	Pore size BJH (Å)
SBA-15	na	na	580	0.1	0.9	61.2
Ti-G-80	80	85.3	572	0.08	0.91	63.2
Ti-G-20	20	21.4	513	0.004	0.8	63.6
Ti-G-10	10	14.5	447	0.08	0.71	59.2
Au/Ti-G-80	80	88.2	499	0.05	0.87	65.0
Au/Ti-G-20	20	23.2	439	0.05	0.74	63.0
Au/Ti-G-10	10	16.1	407	0.04	0.68	61.5
Ti-H-80	80	2033	631	0.1	0.98	63.0
Ti-H-40	40	1233	633	0.1	0.9	61.0
Ti-H-20	20	599	568	0.1	0.93	60.5
Ti-H-10	10	4824	608	0.11	0.93	58.8
Au/Ti-H-80	80	2330	531	0.04	0.9	65.3
Au/Ti-H-40	40	1256	545	0.03	0.9	62.2
Au/Ti-H-20	20	712	526	0.04	0.9	62.0
Au/Ti-H-10	10	5354	470	0.03	0.78	60.0

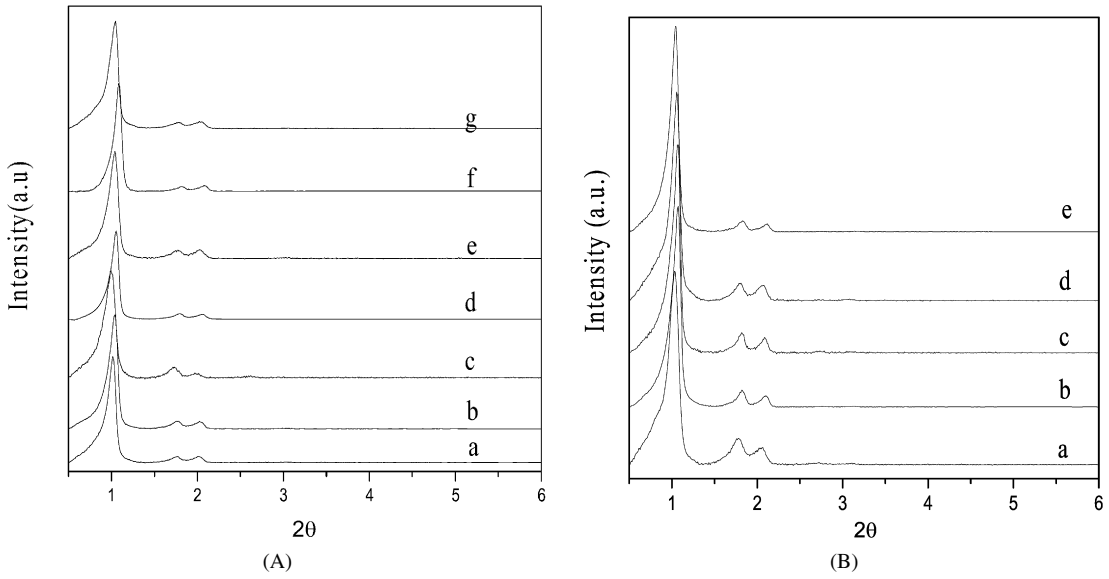

Fig. 1. XRD patterns: (A) (a) pure silica SBA-15, (b) TiG-80, (c) TiG-40, (d) TiH-40, (e) TiG-20, (f) TiH-20 and (g) Ti-G-10; (B) (a) Au/TiH-80, (b) Au/TiH-40, (c) Au/TiH-20, (d) Au/TiG-20 and (e) Au/TiG-10.

3. Results and discussion

3.1. XRF analysis

Elemental analysis of the calcined powders reveals the actual amounts of titanium incorporated into the SBA-15 framework (Table 1). All of the Au/Ti-SBA-15 samples prepared by the grafted method exhibit a final Si/Ti molar ratio close to the target loading. XRF results for the direct synthesized Au/Ti-SBA-15 materials show very low titanium content in the final products, comparable with that of the grafted samples. UV–vis analysis of the filtrate (not shown) of the hydrothermally synthesized materials demonstrates that most of the titanium was not incorporated into the SBA-15 structure and washed out. The gold loading for all of the catalysts was always close to the target loading, and the amount of chloride was below the detection limit.

3.2. X-ray diffraction

The XRD patterns of the synthesized materials are typical for the SBA-15 [29]. Fig. 1A illustrates the presence of peaks at 2θ angle of 1.01°, 1.74°, and 2.01°, corresponding to the (100), (110), and (200) Bragg reflections, confirming the hexagonal symmetry (P6mm) of the SBA-15 materials prepared. A well-resolved peak at 1.02° and two other peaks at 1.75° and 2.05° also can be seen for the Ti-SBA-15 (Fig. 1A) and Au/Ti-SBA-15 samples (Fig. 1B), respectively. The incorporation of Ti and Au did not significantly change the hexagonal ordering of the SBA-15 framework. No peak for Au metal at 38.19° can be seen in the XRD patterns. The absence of this reflection indicates that the Au particle size is too small and thus not visible in our data.

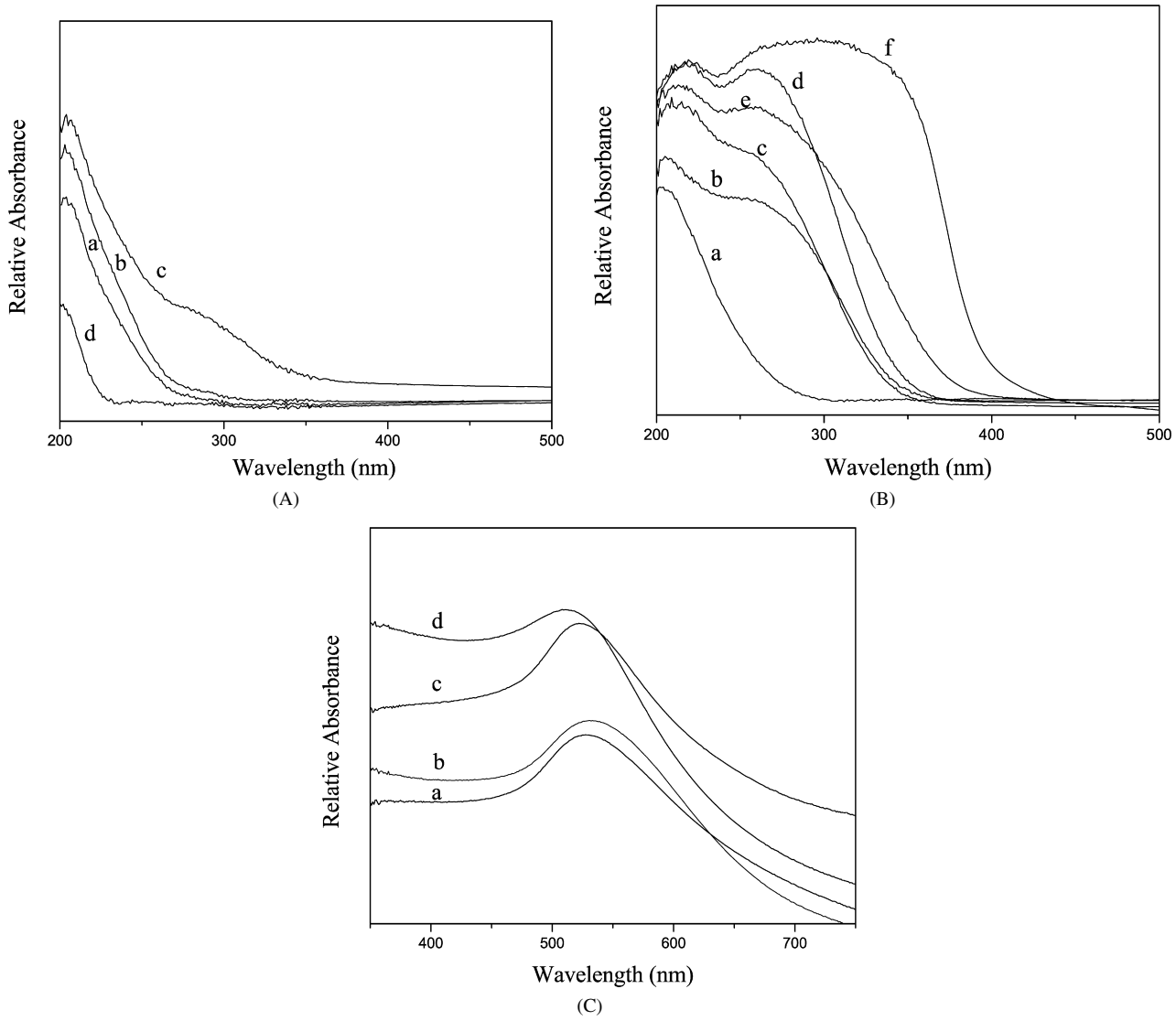

Fig. 2. Diffuse reflectance UV–vis spectra of (A) Ti-H-*n* sample with different molar ratio Si/Ti of (a) 80, (b) 40, (c) 20 and (d) 10; (B) Ti-G-*n* sample with different molar ratio Si/Ti of (a) TS-1 as tetrahedral reference, (b) 80, (c) 40, (d) 20, (e) 10, (f) TiO_2 anatase; (C) (a) Au/Ti-G-40, (b) Au/Ti-G-20, (c) Au/Ti-H-40 and (d) Au/Ti-H-20.

3.3. UV–vis diffuse reflectance spectroscopy

Diffuse reflectance spectroscopy in the UV–vis region is a sensitive method for characterizing the coordination environment of Ti in SBA-15. The UV–vis spectra of the TiH-*n* and TiG-*n* samples, TS-1 (tetrahedral reference), and TiO_2 anatase phase are given in Figs. 2A and 2B. The catalyst samples prepared by the direct synthesis method (Fig. 2A) with different Si/Ti molar ratios show an intense absorption band at 208 nm, assigned to the ligand-to-metal charge transfer from oxygen to Ti of an isolated tetrahedral Ti species [36]. For the sample with a Si/Ti ratio of 20, along with this band, a shoulder with a maximum around 257 nm can be seen, possibly due to the presence of Ti atoms in fivefold and sixfold coordination. These are probably generated on hydration by one or two water molecules of a tetrahedral titanium ion in the first coordination sphere [37]. The hydrophilic surface and high surface area of SBA-15 material yield a high water adsorption capacity, leading to hydration of surface Ti ions.

Fig. 2B displays the UV–vis spectra obtained for the Ti-SBA-15 samples prepared by the grafting method. All of these samples have a UV band at around 208–218 nm. This can be related to the tetrahedral Ti sites or to a distorted tetrahedral environment, which is a direct consequence of the amorphous nature of the walls of the mesoporous material [37]. With an increase in Ti loading from 80 to 10 Si/Ti molar ratio, the UV–vis spectra became broader in the high-wavelength region, indicating that the Ti atoms were no longer completely isolated in the SBA-15 structure. A shoulder at around 330 nm would be expected in the UV–vis spectrum if the catalyst samples contained some bulk titanium oxide [36].

After gold deposition–precipitation in the Ti-SBA-15 support materials prepared by the two methods of Ti incorporation and consecutive calcination in air at 400 °C, it was observed

that all materials attained a pink color typical of the presence of Au nanoparticles. These materials had a characteristic absorption band in the visible region of the electromagnetic spectrum at around 520–550 nm (Fig. 2C). This absorption band was due to surface plasmon vibrations, which are dependent on the gold particle size and the support oxide used [38].

3.4. N_2-sorption measurements

Isotherms of the nitrogen adsorption–desorption experiments of the calcined materials and the related pore size distribution curves calculated using the BJH method [39] are shown in Figs. 3A and 3B. The BET surface area, micropore volume, BJH mesopore volume, and pore sizes of these materials are given in Table 1. The isotherms for SBA-15 silica and Ti-SBA-15 sample presented in Fig. 3A exhibit a H1 hysteresis loop of type IV, according to the IUPAC classification and are typical of materials with cylindrical mesopores [40]. All isotherms show a sharp inflection in the adsorption branch at a relative pressure of about 0.72. This is characteristic of capillary condensation within uniform pores. A good match between the points of inflection of the adsorption branch of each isotherm suggests that all the samples have similar pores (Fig. 3A). The pore size distribution curves shown in Fig. 4A present an average pore size of about 62 Å for the Ti-H-*n* samples, whereas in the case of the Ti-G-*n* samples, partial pore blocking results from increasing the titanium content (Fig. 4B).

The introduction of Au nanoparticles in the SBA-15 support materials resulted in a much broader hysteresis loop, as illustrated in Fig. 3B. The presence of the Au nanoparticles caused a shift in the desorption branch to lower pressures, whereas the adsorption branch was only affected slightly. This adsorption–desorption behavior has been shown to be consistent with a structure comprising open and closed/blocked cylin-

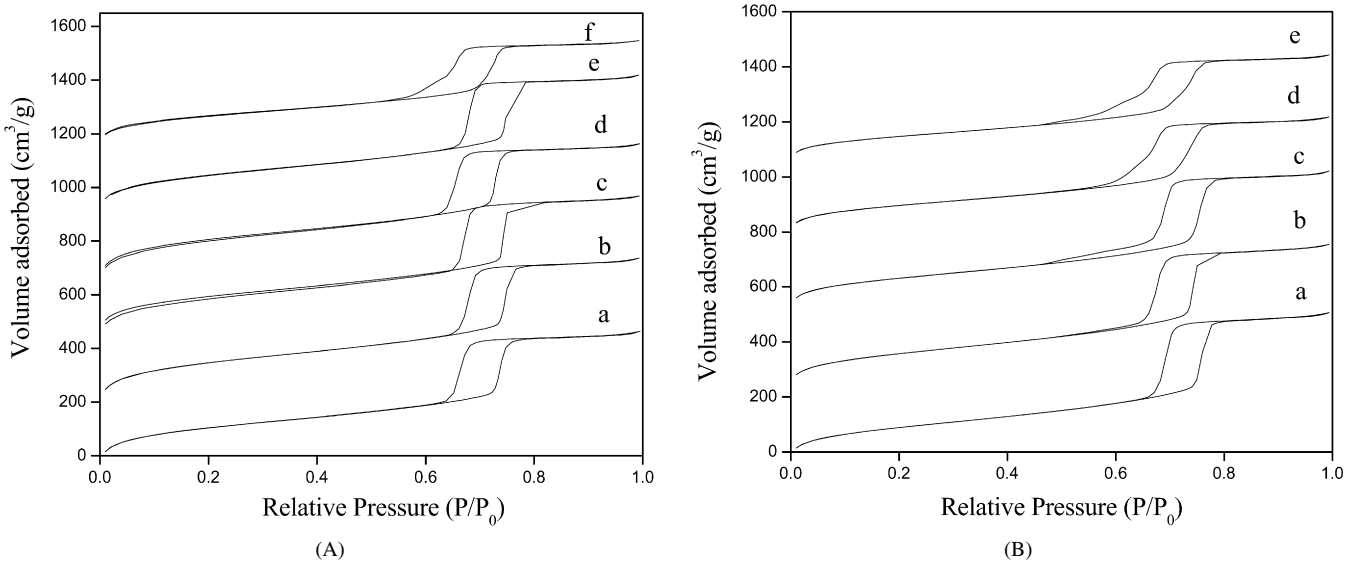

Fig. 3. Nitrogen adsorption–desorption isotherms for (A) (a) SBA-15, Ti-H-*n* sample with molar ratio Si/Ti of (b) 80, (c) 20, (d) 10 and Ti-G-*n* sample with molar ratio Si/Ti of (e) 80 and (f) 10; (B) Au/Ti-H-*n* of (a) 80, (b) 40 and Au/Ti-G-*n* of (c) 80, (d) 20 and (e) 10.

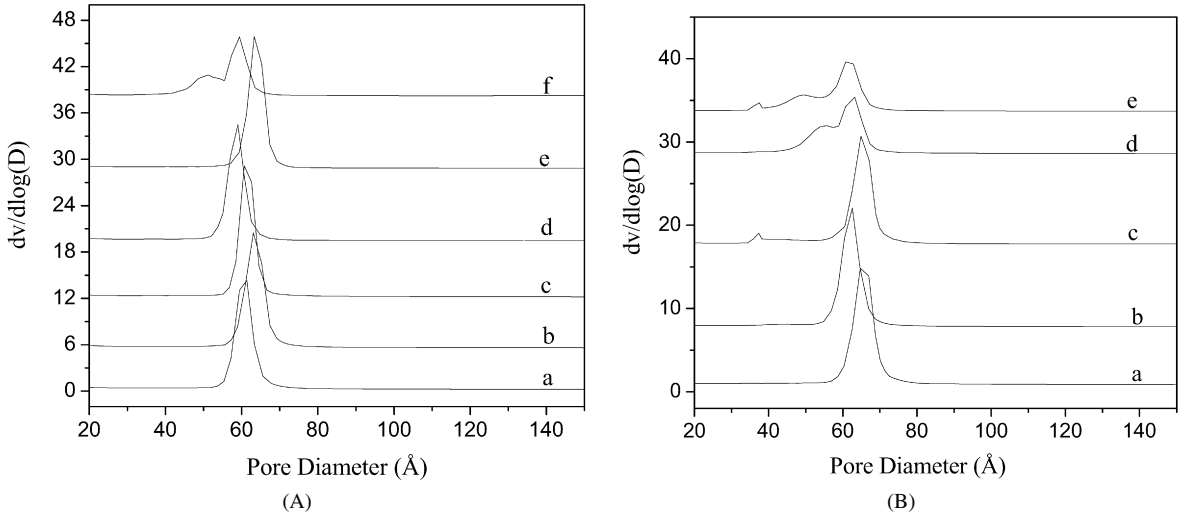

Fig. 4. Pore size distribution of (A) (a) SBA-15, (b) Ti-H-80, (c) Ti-H-20, (d) Ti-H-10, (e) Ti-G-80 and (f) Ti-G-10; (B) (a) Au/Ti-H-80, (b) Au/Ti-H-40, (c) Au/Ti-G-80, (d) Au/Ti-G-20 and (e) Au/Ti-G-10.

drical mesopores [41,42]. The additional features in Fig. 4B at 50–55 Å can be ascribed to partial pore blocking of the pores of the Ti-SBA-15 materials by Au nanoparticles. This blockage increases significantly with increasing titanium loading, as shown in Fig. 4A for sample Au/Ti-G-10.

3.5. Transmission electron microscopy

Fig. 5 shows some TEM micrographs of the samples under investigation. More specifically, Fig. 5a presents a TEM micrograph of the SBA-15 starting material, showing a uniform hexagonal structure, completely consistent with the corresponding XRD data. The TEM micrographs of the Ti-modified SBA-15 samples, illustrated in Figs. 5b and 5c, show no significant changes in spacing between the SBA-15 channels, suggesting that the inclusion of Ti in the SBA synthesis mix or the grafting process does not adversely affect the integrity of the SBA-15 structure. After deposition of Au (Figs. 5d and 5e), the Au particles are smaller on average in the hydrothermally prepared sample (Fig. 5d) than in the corresponding grafted sample (Fig. 5e). The other interesting point is that the Au particles seem to extend along the lengths of the mesopore channels; however, it appears that some of the Au particles are larger than the mesopore channels, which may suggest that (a) the Au particles expand across the mesoporous wall or (b) some Au nanoparticles seems to be formed on the surface of the support.

To elaborate further on this point, Fig. 6 shows the size distribution of the gold nanoparticles observed for both the Au/Ti-

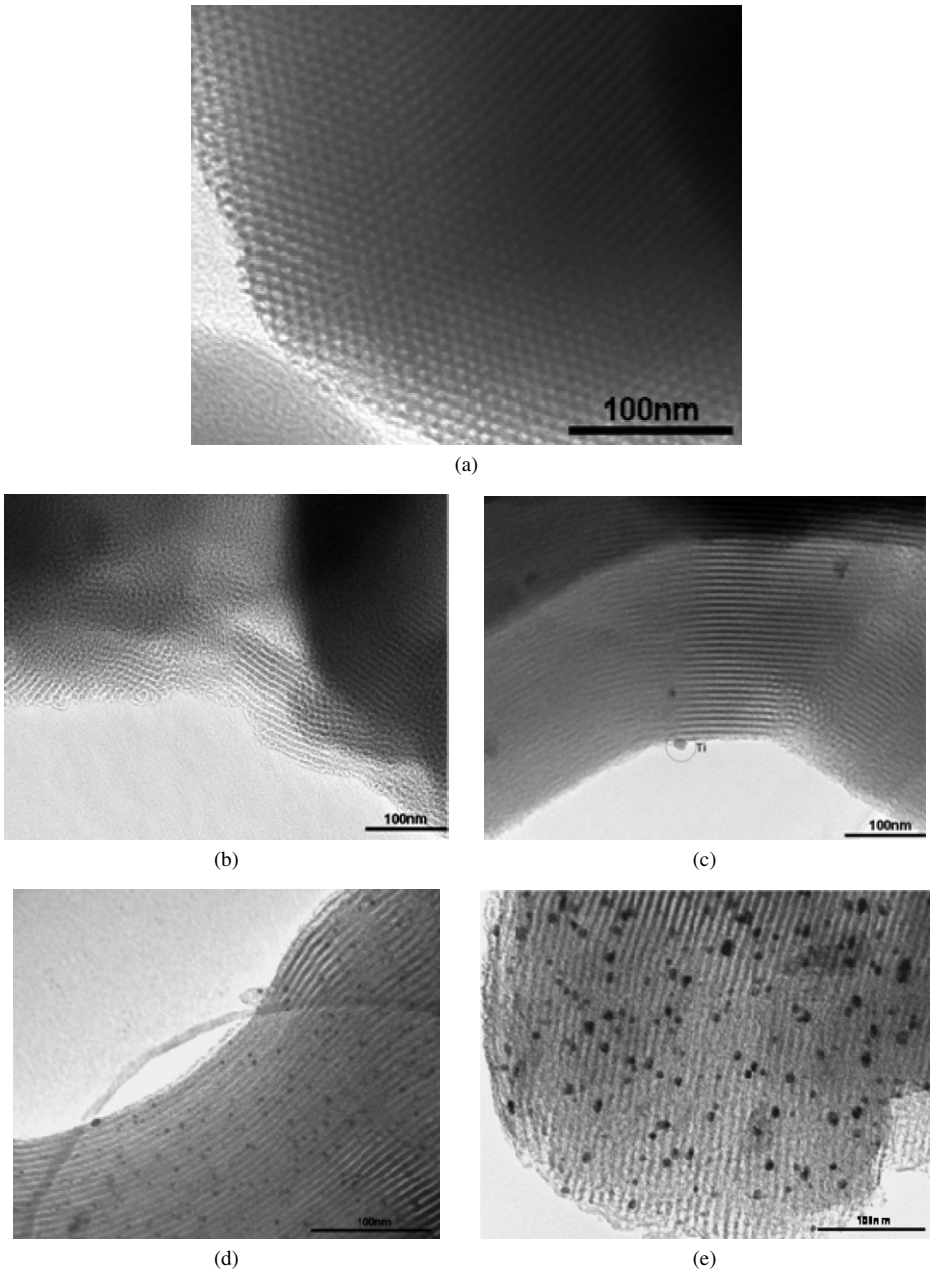

Fig. 5. Transmission electron micrograph of (a) SBA-15, (b) Ti-H-20, (c) Ti-G-20, (d) Au/Ti-H-20 and (e) Au/Ti-G-20. Note that the Ti-G-20 sample contains small amorphous Ti particles.

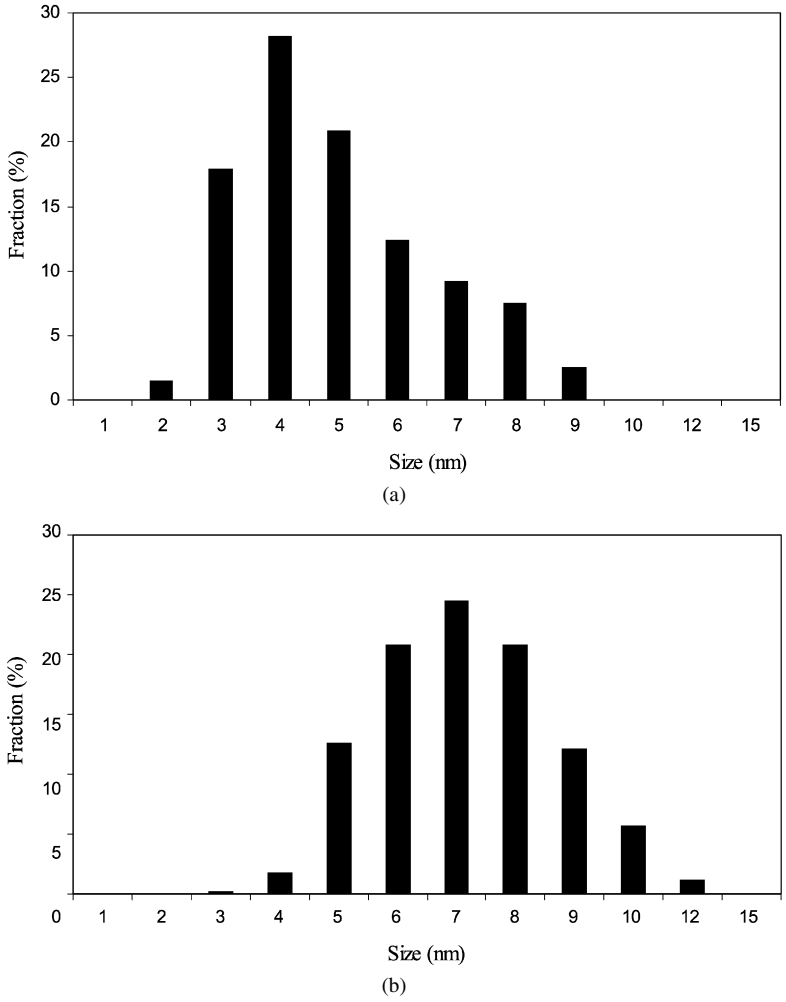

Fig. 6. Size distribution plot of supported Au nanoparticles in (a) Au/Ti-H-20 and (b) Au/Ti-G-20.

G-20 and Au/Ti-H-20 samples. From the metal particle size distributions, it can be concluded that for the hydrothermally prepared sample, the gold nanoparticles are smaller on average (4.45 nm) than those formed in the grafted sample (6.58 nm). The N_2-sorption and XRD measurements show that apart from the presence of titanium, the support oxides are almost identical. Considering that the samples were prepared identically, this difference must be caused by a difference in interaction between the metal and the support oxide. It is also seen that smaller gold particles are formed for silica-supported gold catalysts compared with identically prepared titania-supported gold catalysts [43]. Because our catalyst did not exhibit significant sintering of gold during the reaction and regeneration, it must be concluded that the different gold particle size originates from the preparation procedure, in which nucleation and particle growth must be different when titanium is present in the SBA-15 material.

3.6. Ti K-edge X-ray absorption spectroscopy

To determine the local coordination chemistry of Ti^{4+} in the different catalyst materials, X-ray absorption spectroscopy measurements were performed at the Ti K-edge. The near-edge region in the XANES spectra provides valuable information on the environmental geometry of the absorbing atom (i.e., Ti). Indeed, for Ti^{4+}, the position and intensity of the pre-edge peak due to a 1s–3d transition is related to its coordination environment. The feature above the Ti K-edge is attributed to a 1s–4p transition and a decrease in the pre-edge intensity correlates with an increase of the feature corresponding to the 1s–4p transition. This may provide evidence of increased formation of pentagonal, distorted octahedral, and octahedral coordinated Ti centers [44–46].

Where Ti^{4+} is tetrahedrally substituted or grafted into/onto a silica matrix, the position of the peak when using a Si (111) monochromator appears to remain consistently around 4969.2 eV (Fig. 7), but its intensity can vary. For example, Thomas and Sankar [44] showed that whereas numerous samples, including $Ti(OSiPh_3)_4$ and $C_6H_{11}Si_7O_{11}Ti–O–X$ (where $X = SiPh_3$) have been shown crystallographically to contain tetrahedral Ti^{4+} species, the XANES peak at 4969.2 eV has an intensity of 0.85 and 0.61, respectively. Perhaps more significantly for our work, grafted Ti samples on mesoporous MCM-41 type structures give a pre-edge intensity (for a calcined/dehydrated sample) close to 0.65 [45,47]. Fig. 7 plots of the 1s–3d peak intensity versus the pre-edge energy position

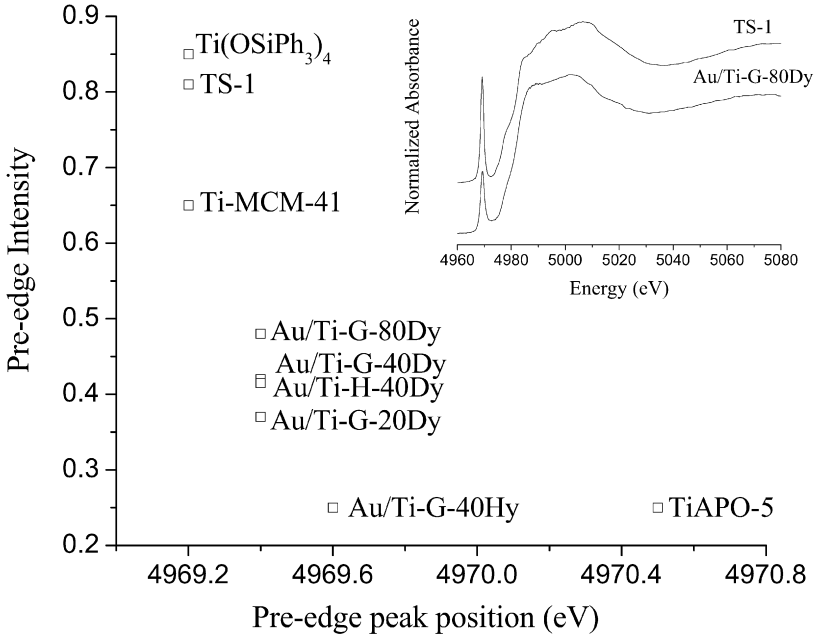

Fig. 7. Variation of the pre-edge peak intensity for several titanium-containing Au/Ti-SBA-15 catalysts, as well as some reference compounds (TS-1, TiAPO-5, Ti-MCM-41 and $Ti(OSiPh_3)_4$) (Dy—dehydrated, Hy—hydrated).

for some of our samples in relation to three standard materials, including a reference compound containing framework-substituted tetrahedral Ti^{4+} (TS-1), the predominantly octahedral Ti^{4+}-containing reference sample TiAPO-5, and the Ti-MCM-41 sample reported previously [45,47,48]. For dehydrated samples, the position of the 1s–3d peak was found to be shifted in energy by 0.2 to 4969.4 eV relative to the tetrahedral containing Ti^{4+} standards and to have lower intensities. From these observations, it is possible to conclude that the coordination of Ti^{4+} within these samples is likely to be higher than 4, suggesting that a mixture of both tetrahedral and higher coordinated (5 and 6) titanium species are present. However, the relative amounts of each of these species appear to vary, because the intensity decreases with increasing titanium loading.

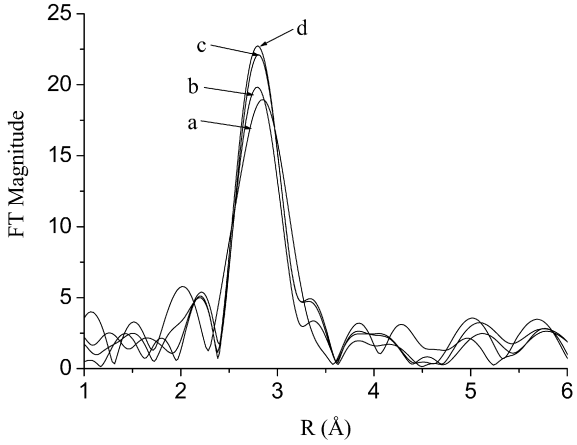

Fig. 8. Comparison of the Fourier-transformed EXAFS data of (a) Au/Ti-H-20, (b) Au/Ti-G-80, (c) Au/Ti-G-40 and (d) Au/Ti-G-20.

3.7. Au L_{III}-edge X-ray absorption spectroscopy

Fig. 8 shows the Fourier transforms (FTs) for the Au/Ti-SBA-15 materials with the corresponding data determined from the least squares fitting process shown in Table 2. An initial evaluation of Fig. 8 shows that the FT magnitudes of the samples increase with increasing titanium oxide loading. In addition, the general profiles of the Au/Ti-G samples appear similar to one another but different than the Au/Ti-H sample. Most notably, for the Au/Ti-H-20 sample, the largest peak at ca. 2.85 Å due to Au–Au scattering appeared much broader then in the Au/Ti-G samples, suggesting a rather broad particle size distribution in this sample. Closer inspection of the data obtained after analysis confirms the relationship between the average Au–Au coordination number and the titanium loadings of the Au/Ti-SBA-15 materials. In particular, a N_1 value of 7.8 (±0.78) was obtained for the lowest titanium-loaded sample Au/Ti-H-20, whereas a N_1 value of 9.7 (±0.97) was obtained for the Au/Ti-G-20 material containing the most titanium. Because it is well known that for small particles (ca. <50 Å), the relationship between the particle diameter and coordination number is a strong and nonlinear function, it would appear that the lower titanium-loaded sample, Au/Ti-H-20, has the smallest gold particles. Further proof for these observations can be seen by comparing the first shell near-neighbor distances where a 0.7% contraction of the average N_1 Au–Au distance was observed in the Au/Ti-H-20 relative to that of the foil [49]. An estimation of the particle size from the N_1 coordination numbers suggests that the particle size ranges from 14 to 30 Å, which is typically some ∼30 Å lower than the average size determined from TEM imaging. Because EXAFS is a more "volume-sensitive" technique, it is possible that these systems are more polydis-

Table 2
EXAFS fit parameters for different Au/Ti-SBA-15 samples compared with Au foil and Au/TiO_2 reference materials (with k^3 weighting: $\Delta k = 4.3$–17.0 Å^{-1} and $\Delta r = 0$–6.0 Å; na = not applicable)

Sample and coordination shells	Au–Au distance (Å)	Coordination number	Debye–Waller ($2\sigma^2$ Å^2)[a]	E_f (eV)	Particle size estimate (Å)	N_3/N_1 ratio	R (%)[a]
Au foil							27.5
N_1	2.86	12	0.016	−6.2	na	2	
N_2	4.06	6	0.023				
N_3	4.99	24	0.027				
Au/Ti-G-80							31.6
N_1	2.84	7.9	0.016	−7.9	15	0.87	
N_2	4.06	3.4	0.023				
N_3	4.99	6.9	0.027				
Au/Ti-G-40							29.7
N_1	2.85	9.6	0.016	−7.3	28	1.33	
N_2	4.06	4.1	0.023				
N_3	4.97	12.2	0.027				
Au/Ti-G-20							32.2
N_1	2.85	9.7	0.016	−6.7	28	1.29	
N_2	4.05	4.1	0.023				
N_3	4.97	11.9	0.027				
Au/Ti-H-20							30.3
N_1	2.84	7.8	0.016	−8.5	14	0.79	
N_2	4.03	3.4	0.023				
N_3	4.94	6.3	0.027				
Au/TiO_2							35.9
N_1	2.84	8.1	0.016	−8.1	15	1.3	
N_2	4.07	3.38	0.023				
N_3	4.97	10.64	0.027				

[a] Due to correlation problems the Debye–Waller factors reported for the samples were extracted from fitting the foil data and were not refined.

perse than suggested by the TEM imaging because the EXAFS shows a greater sensitivity toward species that cannot be seen by TEM [50]. We also note that the estimation is based on the assumption that the particles are essentially spherical/cuboctahedral, although it has also been shown that the N_1 values for different shapes with similar sizes do not differ significantly [51–53]. However, it has been previously suggested that the ratio between the third and first coordination numbers can be used to obtain geometric information on the particles [53]. Interestingly, we see very similar values for this ratio in all but one of the Au/Ti-G samples (∼1.3) (Table 2), which was previously proposed to be indicative of distorted cubic or slab-like structures in which two of the dimensions that describe particle size are similar, whereas the third dimension is significantly different. For the Au/Ti-H-20 and Au/Ti-G-80 samples, a lower ratio (ca. 0.8) was obtained, possibly reflecting a more extreme elongation but more likely due to the particles being smaller. Indeed, despite the sensitivity of the XAS toward smaller species, there does appear to be some correlation with the TEM images, in which many of the gold particles appear to be elongated along the length of the channels.

3.8. Catalytic performance

The catalytic performance of the different Au/Ti-SBA-15 catalyst materials under study were tested for the direct epoxidation of propene. Conversion, selectivity, and hydrogen efficiency results at different reaction temperatures for the grafted and hydrothermally prepared catalysts with Si/Ti molar ratios are summarized in Table 3. Major differences can be seen among the catalysts prepared using different preparation methods. The principal products of the grafted catalysts are propene oxide, acetaldehyde, acrolein, CO_2, H_2O, and propane. The hydrothermally synthesized catalyst materials have a low activity in propene epoxidation, with propane the principal product obtained besides propene oxide. Fig. 9 presents the conversions and selectivities versus temperature for the Au/Ti-H-40 and Au/Ti-G-40 samples. It can be seen that catalytic conversion increases with increasing reaction temperature, but selectivity decreases at higher temperatures. Interestingly, Au/Ti-G-40 has a greater activity than Au/Ti-G-20. Because the reaction rate in Fig. 9 did not increase exponentially with temperature, we checked to verify that the measurements were not performed in a mass-transfer limited regime. Calculation of the Carberry number and Weisz criterion [54] resulted in values of 10^{-6} and 10^{-9}, respectively. Based on these values, we can conclude that the reaction is not internally or externally mass transfer-limited. The nonexponential increase in the reaction rate can be explained by an insufficiently short lifetime of one of the reaction intermediates on the catalytic surface in the complex kinetic network [43]. Most likely, this is related to decomposition of the hydroperoxide intermediate, because the water production rate does increase exponentially with temperature.

Table 3
Overview of the catalytic performances of the Au/Ti-SBA-15 catalyst samples under study

Catalyst	Temperature (°C)											
	50			80			120			150		
	Conv. (%) C_3H_6	PO sel. (%)	H_2 eff. (%)	Conv. (%) C_3H_6	PO sel. (%)	H_2 eff. (%)	Conv. (%) C_3H_6	PO sel. (%)	H_2 eff. (%)	Conv. (%) C_3H_6	PO sel. (%)	H_2 eff. (%)
Au/Ti-H-20	0	0	0	0.25	24	0.27	0.41	19.2	0.15	0.54	52	0.32
Au/Ti-H-40	0	0	0	0.06	28.6	0.22	0.21	27	0.1	0.39	54	0.25
Au/Ti-G-20	0	0	0	0.1	87.5	6.5	0.4	83.5	8.8	0.55	64.7	4.2
Au/Ti-G-40	0.02	100	8.12	0.16	98.3	9.1	0.48	96.5	9.23	0.65	88	4.5
Au/Ti-G-80	0.04	100	5.39	0.3	95.2	6.65	0.7	91.41	5.6	1.1	83.7	4
Au/TiO_2	0.26	99.2	12.02	0.11	89.19	3.72	0.19	29.9	0.32	2.32	0.47	0.01

(Conversions and selectivity values reported are average values taken from 30–270 min within one epoxidation cycle.) Pressure 1 bar, GHSV ($m^3/m^3/h$), 1765 h^{-1} for Au/Ti-SBA-15 catalysts, 5000 h^{-1} for Au/TiO_2 catalyst.

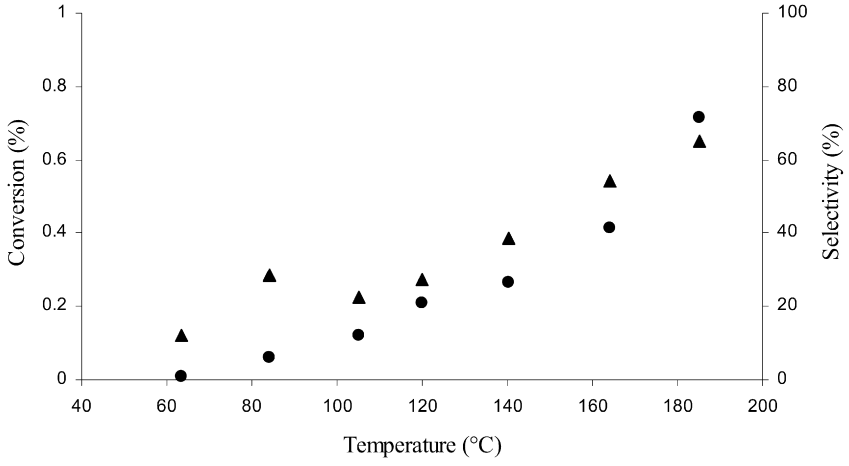

(a)

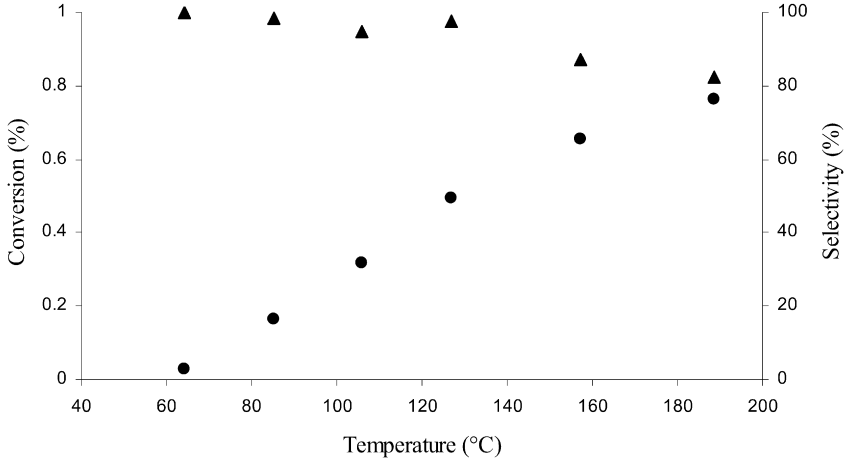

(b)

Fig. 9. Catalytic performance of (a) Au/Ti-H-40 and (b) Au/Ti-G-40 (conversion (●) and selectivity (▲)).

3.9. Catalyst stability

The catalyst materials were tested in successive hour cycles including an intermediate regeneration procedure. Fig. 10 shows the catalytic performance of the Au/Ti-G-40 catalyst. Small losses in catalytic activity can be seen within a cycle, whereas the activity can be almost completely restored during regeneration at 300 °C in oxygen/helium. Compared with

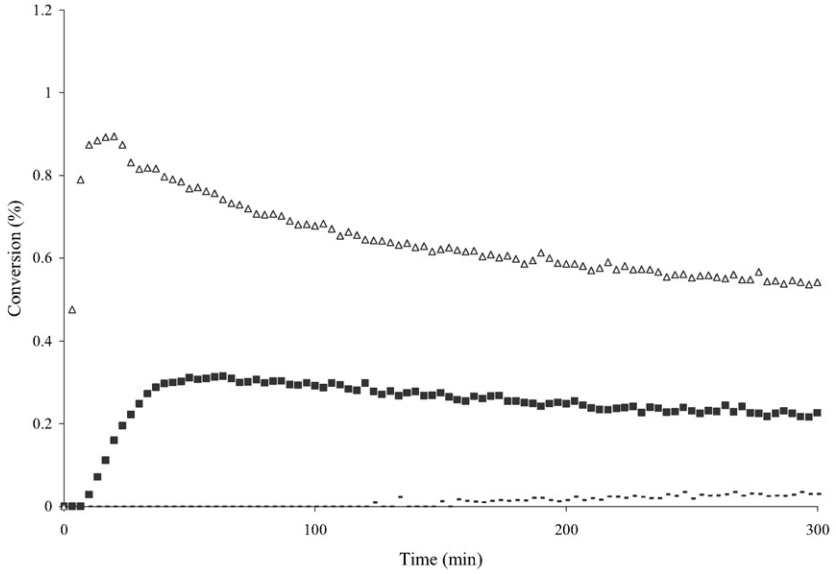

Fig. 10. Catalytic performance of Au/Ti-G-40 catalyst. Conversion at 50 °C (- - -), 100 °C (■), 150 °C (△). Pressure 1 bar, GHSV ($m^3/m^3/h$), 1765 h^{-1}.

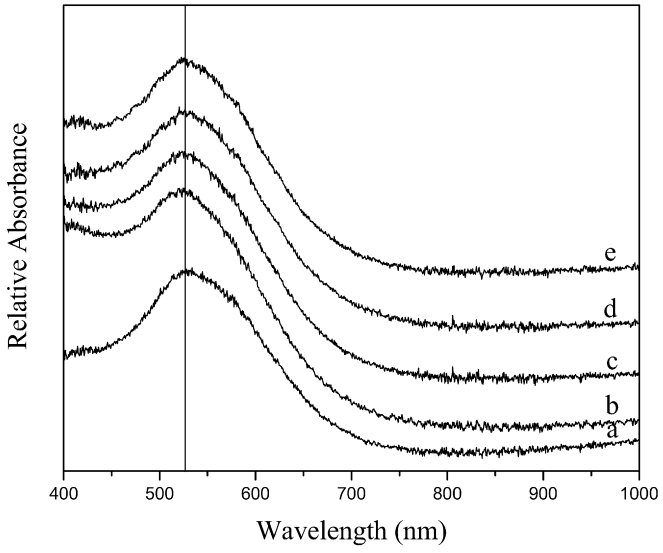

Fig. 11. In situ UV–vis spectra of Au/Ti-G-40 catalyst. (a) Fresh catalyst; epoxidation reaction at (b) 80, (c) 100, (d) 150, (e) 200 °C. Note that after each reaction, a regeneration procedure has been made.

the Au/TiO_2 catalysts reported by Nijhuis et al. [43], Au/Ti-SBA-15 catalysts are more stable during the propene epoxidation reaction. We argue that the stability of Au/Ti-SBA-15 catalysts is related to the presence of isolated Ti in the SBA-15 framework. During the epoxidation reaction, the catalyst was monitored by in situ UV–vis measurements. The similarity of the UV–vis spectra in Fig. 11 indicates that no detectable changes in the nature of the gold particles were seen during these experiments. Finally, Fig. 12 shows a TEM micrograph of a Au/Ti-G-40 catalyst after 14 activity–regeneration cycles. No sintering of supported Au nanoparticles can be seen, ensuring stability of the catalyst materials during catalytic operation.

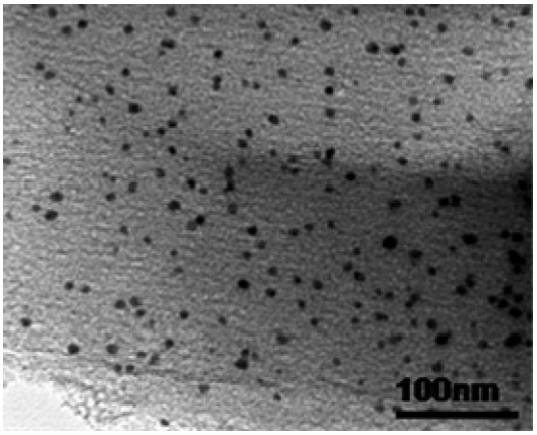

Fig. 12. Transmission electron micrograph of a spent Au/Ti-G-40 catalyst.

3.10. Relating catalyst preparation and structure to propene epoxidation activity

As discussed before, Haruta et al. [26,27] have shown that the selectivity of gold-based catalysts toward propene oxide is dependent on the gold particle size. Thus, gold nanoparticles smaller then 2 nm hydrogenate propene and those between 2 and 5 nm selectively epoxidize propene to propene oxide. Characterization results of the Au/Ti-SBA-15 samples prepared via hydrothermal synthesis show a small amount of titanium compared with the samples prepared via grafting. Moreover, the supported Au nanoparticles are smaller in the hydrothermally synthesized catalyst than in the grafted Au/Ti-SBA-15 catalysts. Considering the characterization results, the differences in catalytic activities in the epoxidation of propene can be linked to the amount of well-dispersed titanium present in the sample, as well as to the gold particle size [21]. Characterization of these catalysts by UV–vis diffuse reflectance spectroscopy and XANES showed that the Au/Ti-G-*n* catalysts contain a higher

absolute amount of isolated tetrahedral titanium than the Au/Ti-H-*n* samples. This suggests that the coordination state of Ti species may be one factor affecting the activity of Au/Ti-SBA-15 catalysts. Another factor is the Au particle size. The Au/Ti-G-40 sample contains larger particles and is more selective to propene oxide than the Au/Ti-G-80 sample. Considering that Au and Ti are the active sites in propene epoxidation, the increase in propene yield for Au/Ti-G-40 can be linked to the greater amount of isolated titanium in a tetrahedral environment, which can favor the desorption of propene oxide The acidity of the support oxide, accessibility of Ti species, and Au particle size also can affect the catalytic performance.

4. Conclusion

Au/Ti-SBA-15 catalysts were prepared with Ti incorporated through either hydrothermal synthesis or grafting. XRD confirmed the integrity of the hexagonal structure of SBA-15 material after Ti (resp. Au) incorporation. XRF showed that the hydrothermal method used to incorporate Ti into the SBA-15 structure resulted in materials with very low Ti amounts, whereas the theoretical amount of Ti in the grafted prepared Ti-SBA-15 materials equaled that in the final materials. N_2 sorption showed that the Ti-SBA-15 materials preserved their mesoporous structure, although higher Ti loadings can lead to a decreased order of the SBA-15 framework. The latter was more evident when supported Au nanoparticles were loaded into the Ti-SBA-15 materials. A bimodal pore size distribution was seen with increasing titanium content. UV–vis DRS and XAS measurements confirmed that the amount of tetrahedral Ti decreased with increasing Ti/Si molar ratio. TEM micrographs and Au L_{III}-edge X-ray absorption spectroscopy analysis showed that the Au particle size was dependent on the amount of titanium present. Au nanoparticles were larger in the Au/Ti-SBA-15 grafted samples than in the hydrothermally prepared Au catalysts. The TEM images also showed that for the Ti-grafted Au/Ti-SBA-15, Au nanoparticles were present at higher density on the surface compared with the hydrothermally synthesized materials. Au/Ti-SBA-15 catalysts prepared by Ti grafting were active and stable in propene epoxidation, whereas Au/Ti-SBA-15 materials prepared via direct synthesis with Ti showed very low catalytic activity. This catalytic behavior is related to differences in the amount of dispersed Ti in the SBA-15 structure, as well to differences in Au nanoparticle size.

Acknowledgments

This work was supported by grants from STW/NWO-VIDI (T.A.N), NWO-VICI (B.M.W.), and NRSC-C (B.M.W.). The authors thank NWO for allowing use of the DUBBLE XAFS beamline in Grenoble (France), and C. van de Spek, A. van der Eerden, and A. Mens for performing the TEM, XRF, and N_2-sorption measurements, respectively. They also thank G. Sankar for providing the TiAPO-5 reference used in this work.

References

[1] T.A. Nijhuis, M. Makkee, J.A. Moulijn, B.M. Weckhuysen, Ind. Eng. Chem. Res. 45 (2006) 3447.
[2] T. Hayashi, K. Tanaka, M. Haruta, J. Catal. 178 (1998) 566.
[3] M. Haruta, N. Yamada, T. Kobayashi, S. Iijima, J. Catal. 115 (1989) 301.
[4] Web of Science–Science Citation Index search for publications with keywords "gold" and ("propene" or "propylene") and ("oxidation" or "epoxidation") d.d. 07/07/2006 resulting in 156 relevant citation hits.
[5] E.E. Stangland, K.B. Stavens, R.P. Andres, W.N. Delgass, J. Catal. 191 (2000) 332.
[6] C. Sivadinarayana, T.V. Choudhary, L.L. Daemen, J. Eckert, D.W. Goodman, J. Am. Chem. Soc. 126 (2004) 38.
[7] C. Qi, M. Okumura, T. Akita, M. Haruta, Appl. Catal. A 263 (2004) 19.
[8] A. Zwijnenburg, M. Makkee, J. Moulijn, Appl. Catal. A 270 (2004) 49.
[9] M. Haruta, B.S. Uphade, S. Tsubota, A. Miyamoto, Res. Chem. Intermed. 24 (1998) 329.
[10] Y.A. Kalvachev, T. Hayashi, S. Tsubota, M. Haruta, J. Catal. 186 (1999) 228.
[11] T.A. Nijhuis, B.J. Huizinga, M. Makkee, J.A. Moulijn, Ind. Eng. Chem. Res. 38 (1999) 884.
[12] B.S. Uphade, M. Okumura, N. Yamada, S. Tsubota, M. Haruta, Stud. Surf. Sci. Catal. 130 (2000) 833.
[13] B.S. Uphade, Y. Yamada, T. Akita, T. Nakamura, M. Haruta, Appl. Catal. A 215 (2001) 137.
[14] B.S. Uphade, T. Akita, T. Nakamura, M. Haruta, J. Catal. 209 (2002) 331.
[15] A.K. Sinha, S. Seelan, T. Akita, S. Tsubota, M. Haruta, Appl. Catal. A 240 (2003) 243.
[16] C. Qi, T. Akita, M. Okumura, K. Kuraoka, M. Haruta, Appl. Catal. A 253 (2003) 75.
[17] N. Yap, R.P. Andres, W.N. Delgass, J. Catal. 226 (2004) 156.
[18] E.E. Stangland, B. Taylor, R.P. Andres, W.N. Delgass, J. Phys. Chem. B 109 (2005) 2321.
[19] A.K. Sinha, S. Seelan, S. Tsubota, M. Haruta, Angew. Chem. Int. Ed. 43 (2004) 1546.
[20] C. Qi, T. Akita, M. Okumura, M. Haruta, Appl. Catal. A 218 (2001) 81.
[21] S. Ivanova, C. Petit, V. Pitchon, Appl. Catal. A 267 (2004) 191.
[22] M. Haruta, S. Tsubota, T. Kobayashi, H. Kageyama, M.J. Genet, B.J. Delmon, J. Catal. 144 (1993) 175.
[23] S. Tsubota, D.A.H. Cunningham, Y. Bando, M. Haruta, Stud. Surf. Sci. Catal. 91 (1995) 227.
[24] W. Li, C. Massimiliano, F. Schüth, J. Catal. 237 (2006) 190.
[25] T. Hayashi, K. Tanaka, M. Haruta, J. Catal. 178 (1998) 566.
[26] M. Haruta, M. Date, Appl. Catal. A 222 (2001) 427.
[27] A.K. Sinha, S. Seelan, S. Tsubota, M. Haruta, Top. Catal. 29 (2004) 95.
[28] D. Zhao, J. Feng, Q. Huo, N. Melosh, G.H. Fredrickson, B.F. Chmelka, G.D. Stucky, Science 279 (1998) 548.
[29] D. Zhao, J. Feng, Q. Huo, N. Melosh, B.F. Chmelka, G.D. Stucky, J. Am. Chem. Soc. 120 (1998) 6024.
[30] Y. Chen, Y. Huang, J. Xiu, X. Han, X. Bao, Appl. Catal. A 273 (2004) 185.
[31] P. Wu, T. Tatsumi, Chem. Mater. 14 (2002) 1657.
[32] Z. Luan, E.M. Maes, P.A.W. van der Heide, D. Zhao, R.S. Czernuszewics, L. Kevan, Chem. Mater. 11 (1999) 3680.
[33] X. Gao, S.R. Bare, J.L.G. Fierro, M.A. Banares, I.E. Wachs, J. Phys. Chem. B 102 (1998) 5653.
[34] V. Parvulescu, C. Anastasescu, C. Constantin, B.L. Su, Catal. Today 78 (2003) 477.
[35] N. Binsted, J.W. Campbell, S.J. Gurman, P.C. Stephenson, EXAFS Analysis Programs, Daresbury Laboratory, Warrington, 1991.
[36] D. Trong On, S. Nguyen, V. Hulea, E. Dumitriu, S. Kaliaguine, Microporous Mesoporous Mater. 57 (2003) 169.
[37] M.S. Morey, S. O'Brien, S. Schwarz, G.D. Stucky, Chem. Mater. 12 (2000) 898.
[38] M.C. Daniel, D. Astruc, Chem. Rev. 104 (2004) 239.
[39] E.B. Barrett, L.G. Joyner, P.P. Halenda, J. Am. Chem. Soc. 73 (1951) 373.

[40] K.S.W. Sing, D.H. Everett, R.A.W. Haul, L. Moscow, R.A. Pierotti, J. Rouquerol, T. Siemieniewska, Pure Appl. Chem. 57 (1985) 603.
[41] P.I. Ravikovitch, A.V. Neimark, Langmuir 18 (2002) 9830.
[42] P. Van Der Voort, P.I. Ravikovitch, K.P. De Jong, M. Benjelloun, E.A. Van Bavel, H. Janssen, A.V. Neimark, B.M. Weckhuysen, E.F. Vansant, J. Phys. Chem. B 106 (2002) 5873.
[43] (a) T.A. Nijhuis, T. Visser, B.M. Weckhuysen, J. Phys. Chem. B 109 (2005) 19309;
(b) T.A. Nijhuis, B.M. Weckhuysen, Chem. Commun. (2005) 6002;
(c) T.A. Nijhuis, T.Q. Gardner, B.M. Weckhuysen, J. Catal. 236 (2005) 153;
(d) T.A. Nijhuis, T. Visser, B.M. Weckhuysen, Angew. Chem. Int. Ed. 44 (2005) 1115.
[44] F. Farges, G. Brown, J. Rehr, J. Geochim. Cosmochim. Acta 60 (1996) 3023.
[45] J.M. Thomas, G. Sankar, Acc. Chem. Res. 34 (2001) 571.
[46] D. Gleeson, G. Sankar, C.R.A. Catlow, J.M. Thomas, G. Spanó, S. Bordiga, A. Zecchina, C. Lamberti, Phys. Chem. Chem. Phys. 2 (2002) 4812.
[47] A. Hagen, K. Schueler, F. Roessner, Microporous Mesoporous Mater. 51 (2002) 23.
[48] F. Farges, G.E. Brown, J. Rehr, J. Phys. Rev. B 56 (1997) 1809.
[49] J.T. Miller, A.J. Kropf, Y. Zha, J.R. Regalbuto, L. Delannoy, C. Louis, E. Bus, J.A. van Bokhoven, J. Catal. 240 (2006) 222.
[50] S. Calvin, S.X. Luo, C. Caragianis-Broadbridge, J.K. McGuinness, E. Anderson, A. Lehman, K.H. Wee, S.A. Morrison, L.K. Kurihara, Appl. Phys. Lett. 87 (2005) 233102.
[51] A.I. Frenkel, C.W. Hills, R.G. Nuzzo, J. Phys. Chem. B 105 (2001) 12689.
[52] A. Carlsson, A. Puig-Molina, T.V.W. Janssens, J. Phys. Chem. B 110 (2006) 5286.
[53] A. Jentys, Phys. Chem. Chem. Phys. 1 (1999) 4059.
[54] R.A. van Santen, P.W.N.M. van Leeuwen, J.A. Moulijn, B.A. Averill, Catalysis: An Integrated Approach, Elsevier, Amsterdam, 1999.